SOLAR CELLS

Iodide management in formamidinium-lead-halide–based perovskite layers for efficient solar cells

Woon Seok Yang,[1] Byung-Wook Park,[1] Eui Hyuk Jung,[2] Nam Joong Jeon,[2] Young Chan Kim,[2] Dong Uk Lee,[3] Seong Sik Shin,[2] Jangwon Seo,[2] Eun Kyu Kim,[4]* Jun Hong Noh,[2,5]* Sang Il Seok[1,2]*

The formation of a dense and uniform thin layer on the substrates is crucial for the fabrication of high-performance perovskite solar cells (PSCs) containing formamidinium with multiple cations and mixed halide anions. The concentration of defect states, which reduce a cell's performance by decreasing the open-circuit voltage and short-circuit current density, needs to be as low as possible. We show that the introduction of additional iodide ions into the organic cation solution, which are used to form the perovskite layers through an intramolecular exchanging process, decreases the concentration of deep-level defects. The defect-engineered thin perovskite layers enable the fabrication of PSCs with a certified power conversion efficiency of 22.1% in small cells and 19.7% in 1-square-centimeter cells.

The main interest in inorganic-organic hybrid perovskite materials stems from the huge success of their application in perovskite solar cells (PSCs), which has led to power conversion efficiency (PCE) of >20% (*1*–*5*). To date, several factors, such as architecture, deposition process, and compositional manipulation of the perovskite materials have been probed and altered in attempts to fabricate efficient PSCs (*4*–*10*). Previously, we proposed a bilayer architecture consisting of perovskite-infiltrated mesoporous TiO_2 with thin upper layers to fabricate efficient PSCs (*6*, *7*). Furthermore, we devised a solvent-engineering process, which used a dropwise dripping of an orthogonal solvent during spinning of the perovskite precursor in a mixture of γ-butyl lactone and dimethyl sulfoxide (DMSO) to produce a bilayer architecture with an extremely uniform and dense surface morphology (*7*). This process was successfully repeated and applied to the fabrication of highly efficient PSCs with PCEs of more than 20% (*2*–*4*). Further, we demonstrated the fabrication of efficient PSCs based on formamidinium lead iodide ($FAPbI_3$) using a two-step process based on intramolecular exchange between organic cations and DMSO molecules (*5*).

[1]Perovtronics Research Center, School of Natural Science, and School of Energy and Chemical Engineering, Ulsan National Institute of Science and Technology, 50 UNIST-gil, Eonyang-eup, Ulju-gun, Ulsan 44919, Korea. [2]Division of Advanced Materials, Korea Research Institute of Chemical Technology, 141 Gajeong-Ro, Yuseong-Gu, Daejeon 34114, Korea. [3]NAND Product Engineering Group, SK Hynix Inc., Icheon 17336, Korea. [4]Department of Physics and Quantum Function Research Laboratory, Hanyang University, Seoul 04763, Korea. [5]School of Civil, Environmental and Architectural Engineering, Korea University, Seoul 136-713, Republic of Korea.
*Corresponding author. Email: seoksi@unist.ac.kr (S.I.S.); junhnoh@korea.ac.kr (J.H.N.); ek-kim@hanyang.ac.kr (E.K.K.)

Theoretical calculations have shown that point defects, such as vacancies (V_{MA}, V_{Pb}, and V_I) and interstitials (MA_i, Pb_i, and I_i), are the most likely defects in methylammonium (MA) lead iodide ($MAPbI_3$) perovskites because of their low energies of formation (*11*, *12*). Moreover, cation substitutions (MA_{Pb} and Pb_{MA}) and antisite substitutions (MA_I, Pb_I, I_{MA}, and I_{Pb}) can also form. Although most vacancy defects create shallow electronic levels near the band edges (*11*–*13*), the formation of deep-level defects, such as interstitial and antisite defects, which are responsible for nonradiative recombination centers in perovskite layers, depends on I-poor or I-rich conditions (*11*).

Recombination centers in polycrystalline perovskite layers can also be generated by grain boundaries (GBs) (*14*–*18*), but electron beam–induced current studies (*19*) have shown that GBs are inert toward charge recombination and might even be beneficial for charge separation, as demonstrated by using scanning Kelvin probe force microscopy (*20*). In situ or posttreatment of GBs with, for example, residual PbI_2 (*14*, *21*); 1,2-ethanedithiol (*15*); pyridine (*16*); phenyl-C_{61}-butyric acid methyl ester (*17*); and guanidinium (*18*) improved performance by passivating undercoordinated Pb and I ions. Nevertheless, the observed increases in performance were limited. Internal passivation methods exploiting the balance of halide ions during the processing stage have not yet been reported for perovskite layers, and approaches that would reduce the number of compositional point defects are necessary to achieve further improvements in the performance of PSCs.

Stewart *et al.* (*22*) suggested that a two-step deposition method could suppress the formation of interstitial iodide. In particular, the presence of I-rich tetraiodoplumbates (PbI_4^- species) in the precursor solution, where PbI_2, formamidinium iodide (FAI), and methylammonium iodide (MAI) are dissolved in dimethylformamide (DMF), may be related to the density of defects stemming from interstitial iodine (I_i) and act as charge recombination centers. Nevertheless, a two-step process that used DMSO as the mediator may also result in the formation of $[(Pb_3I_8)_n]^{2n-}$, which is an I-deficient intermediate that is charge-balanced by FA (or MA) (*23*).

We report a two-step deposition method for the fabrication of high-quality perovskite films that uses an optimized dripping solution to reduce the degree of iodide deficiency, which is common with the two-step process. The PSCs fabricated using this method showed remarkably improved performance compared with the control cell. The introduction of additional iodide ions into the dripping solution facilitated the fabrication of a PSC with a certified PCE of 22.1% under 1 sun illumination (100 mW cm^{-2}).

To facilitate an α-phase $FAPbI_3$ perovskite as a light harvester that is stable at room temperature, we manipulated the composition of $FAPbI_3$ by introducing a small amount of $MAPbBr_3$ (*8*). We incorporated $MAPbBr_3$ into $FAPbI_3$ perovskite films using a modified intramolecular exchange process (*5*). PbI_2 and $PbBr_2$ (mole ratio = 95/5) were dissolved in a mixture of DMF and DMSO (80/20, v/v). We first deposited a $PbI_2(PbBr_2)$-DMSO film by spin-coating a PbX_2 (X = I, Br) solution containing PbI_2 and $PbBr_2$ dissolved in a mixture of DMF and DMSO onto a nanocrystalline TiO_2 scaffold. In the second step, a solution of FAI and MABr, containing iodide ions (I^-) dissolved in isopropyl alcohol (IPA), was spin-coated.

To prepare this solution, an iodide solution was first prepared by stirring solid iodine (I_2) in IPA at 80°C. Iodine can be ionized to I^- by oxidation of IPA with the formation of acetone via Eq. 1 (*24*).

$$(CH_3)_2CHOH(IPA) + I_2 \xrightarrow{\Delta}$$
$$(CH_3)_2C=O(acetone) + HI + I^- \quad (1)$$

A continued exergonic equilibrium gives rise to triiodide ions (I_3^-), as shown in Eq. 2:

$$I_2 + I^- \rightleftarrows I_3^- \quad (2)$$

Analysis of the solution of I_2 in IPA by ultraviolet-visible (UV-vis) spectroscopy (fig. S1) (*25*) revealed that the intensities of the absorption peaks at 291 and 361 nm increased during the course of stirring, indicating that $[I_3^-]$ increased as a function of the stirring time through the reactions shown in Eqs. 1 and 2 (*26*), with all iodine eventually converted into the I_3^- after stirring for 7 days. Subsequently, FAI(+MABr) was dissolved in an IPA solution containing 1 to 5 mmol of I_3^- to prepare the dripping solution for perovskite layer formation. After spin-coating, this solution was retained on the surface to induce intramolecular exchange between DMSO and FAI(+MABr), followed by annealing at 150°C. We fabricated PSCs with the following

architecture: FTO/thin-barrier TiO_2 (~60 nm)/mesoporous-TiO_2:perovskite composite layer (~150 nm)/perovskite upper layer (~500 nm)/PTAA (~50 nm)/Au (~100 nm), where FTO is F-doped SnO_2 and PTAA is poly(triarylamine) [fig. S2A (*25*)].

The performance of the PSCs increased with the addition of any I_3^- to the dripping solution, with the maximum performance or "target device" attained when the dripping solution contained 3 mmol of I_3^- (Fig. 1A). The current-voltage (*I-V*) characteristics (Fig. 1B) of the target device were compared with those of the control (no added I_3^-). The target PSC exhibited an open-current voltage (V_{oc}) of 1.1 V, a short-circuit current (J_{sc}) of 24.1 mA·cm^{-2}, and a fill factor (FF) of 81.9%, for a PCE of 21.6%. The control device showed an overall PCE of 20.3% with a V_{oc} of 1.07 V, a J_{sc} of 23.5 mA·cm^{-2}, and a FF of 80.8%. The enhanced J_{sc} value arose from improved light-harvesting capacity rather than increased charge collection, as the thicknesses and surface morphologies of the target and control PSCs are almost identical (fig. S2B) (*25*). Moreover, the proportion of the α-$FAPbI_3$ phase is increased by the addition of I_3^-, as will be evidenced by the UV-vis absorption spectra and the grazing-incidence wide-angle x-ray scattering (GIWAXS) analysis, despite the similar thicknesses. The improvements in both V_{oc} and FF are indicative of improved crystallinity and a smaller number of trapping sites, which are responsible for non-radiative charge recombination of perovskite domains. In particular, the unavoidable introduction of defects into the crystalline lattice during processing increases charge recombination. High crystallinity and preferred orientation, likewise, will influence charge dissociation, transport, and diffusion length considerably (*27*). The J_{sc} value obtained from the *J-V* characteristics is well matched (within 5%) with the external quantum efficiency (EQE) obtained by the integration of the spectral response (Fig. 1C). Nevertheless, the EQE exhibited very interesting features over the spectral range of the device response. Namely, the EQE value is higher at longer wavelengths, most likely from slight changes in the ratio of nonperovskite and perovskite materials between the surface and the interior of the films.

The UV-vis absorption spectra obtained for perovskite thin films deposited using PbI_2 ($PbBr_2$)-DMSO, followed by FAI(+MABr) in IPA solution with and without external I_3, showed very similar absorption profiles but a slightly higher absorption over the entire region below 780 nm in comparison with the control layer (Fig. 1D). This outcome suggests that the proportion of α-$FAPbI_3$ phases increased in the target layer. The fraction of $MAPbBr_3$ in $FAPbI_3$ was estimated to be ~5 mol% from the blue-shift of the onset absorption (*5*). We also conducted GIWAXS analysis using a two-dimensional (2D) detector to probe the orientation and crystallinity of internal layers for the $FAPbI_3$ layers deposited with and without I_3^- with the x-ray incident angle at 0.05° (near surface) or 0.3° (full depth) to the sample (figs. S3 and S4) (*25*). Signals corresponding to PbI_2 disappeared at the lower incident angle (0.05°) and decreased substantially at the higher angle (0.3°) in the target layer relative to the control, but those for both the α- and δ-$FAPbI_3$ increased in intensity in the target layer. The difference between the surface and full-depth diffractions of PbI_2 reflects the reaction between PbI_2-DMSO and FAI(+MABr), which is supplied externally. The formation of $FAPbI_3$ likely occurs via intermediates such as PbI_2-DMSO-FAI(+MABr) and PbI_2-DMSO phases through the two-step process. The intermediate consists of an I-deficient (organic cations)–Pb_3I_8 phase (*23*) or an I-deficient PbI_2-DMSO complex forms because PbI_2 itself is often I-deficient (*28*). Thus, I_3^- in the dripping solution would both increase the proportion of the crystalline α-$FAPbI_3$ phase and reduce the concentration of defects in the entire perovskite layer.

To gain deeper insight into the nature of these defects, we performed deep-level transient spectroscopy (DLTS) (*29*) and steady-state

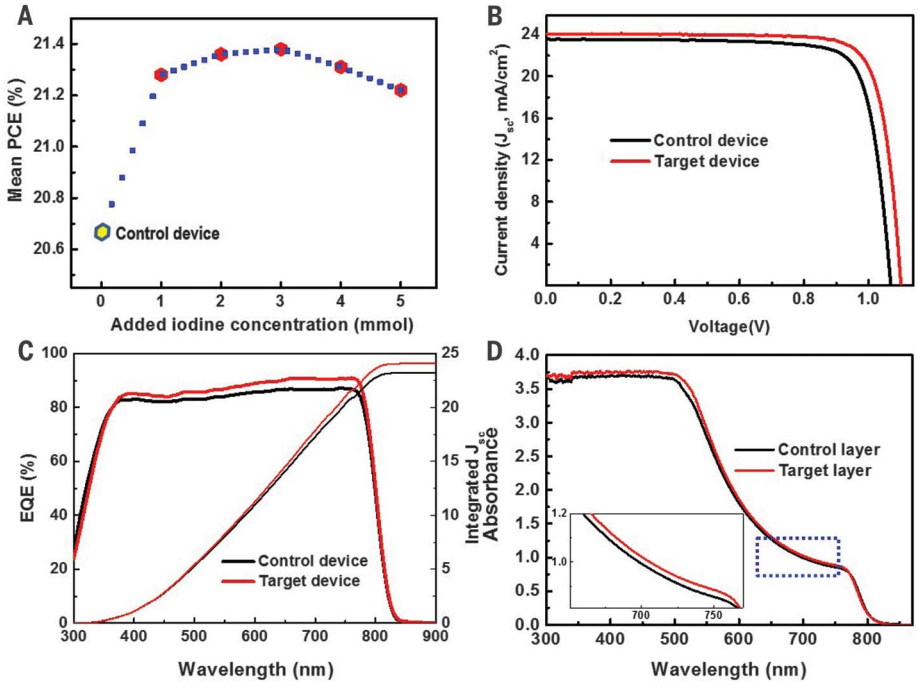

Fig. 1. Device performance analysis and UV-vis absorption spectra of perovskite layers deposited via a two-stage process with and without the addition of triiodide ions into the dripping solution. (**A**) Relation between the relative power conversion efficiency and the concentration of iodide ions added into the dripping solution. (**B**) *J-V* characteristics determined under simulated AM 1.5 G illumination for the control and target devices. (**C**) External quantum efficiency and integrated J_{sc} for the control and target devices. (**D**) UV-vis absorption spectra for the control and target perovskite layers (inset is magnified absorption).

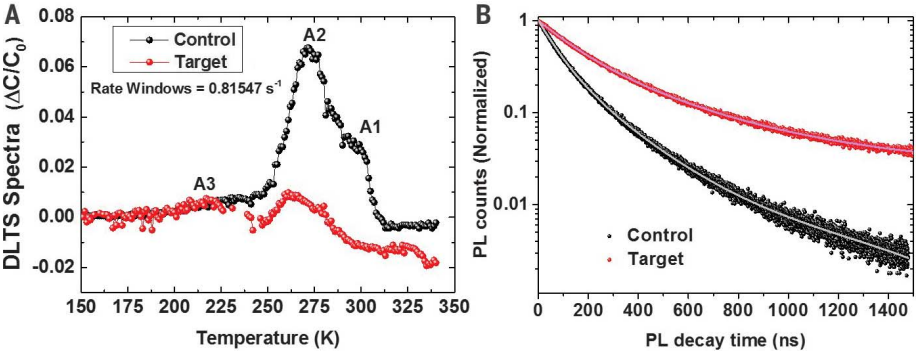

Fig. 2. Deep-level transient spectroscopy (DLTS), and time-resolved photoluminescence (TRPL) measurements. (**A**) DLTS spectra of the control and target layers measured in between 150 K and 330 K. (**B**) TRPL decay curves on the control and target perovskite layers emitted at λ = 825 nm with the biexponential fitting.

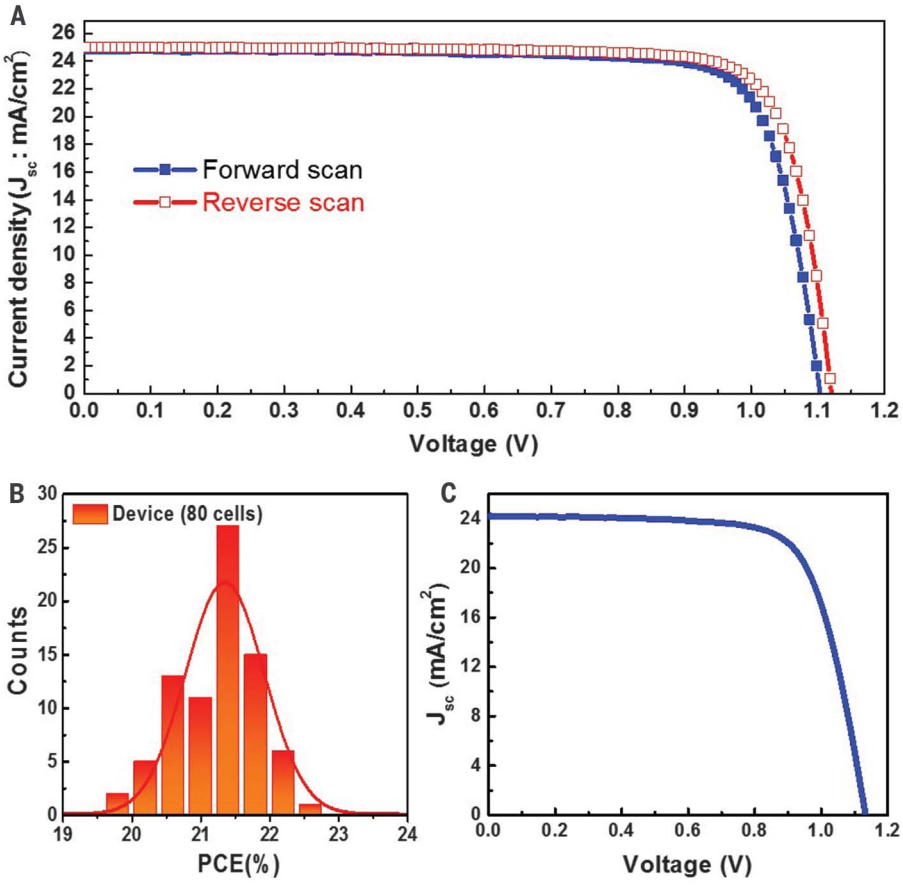

Fig. 3. Current density–voltage (*J-V*) curves and photovoltaic parameters of the best-performing small and large PSCs and device reproducibility. (**A**) *J-V* curves of a small PSC (0.095 cm^2) in forward- and reverse-scan modes and the corresponding photovoltaic parameters. (**B**) Histogram of the average power conversion efficiency determined for 80 PSC devices. (**C**) *J-V* curve for a large PSC (1.0 cm^2) plotted as the average of the reverse- and forward-scan modes and the corresponding photovoltaic parameters.

and time-resolved photoluminescence (PL). The temperature scans for the control layer reveal three defect levels, denoted A1, A2, and A3 (Fig. 2A). The activation energy (E_a) and capture cross-section (E_C) values determined from the Arrhenius plots in fig. S5 (*25*) were E_C of –0.82 eV and 2.47 × 10^{-12} cm^2 in A1, E_C of –0.78 eV and 2.39 × 10^{-12} cm^2 in A2, and E_C of –0.46 eV and 8.65 × 10^{-16} cm^2 in A3, respectively. In the target layer, the A1 signal disappeared readily and the defect concentration for A2 decreased from 5.28 × 10^{14} cm^{-3} to 8.81 × 10^{13} cm^{-3} through interaction with I_3^-. From the disappearance of the A1 peak, we surmise that defect sites located in the A1 level can be easily healed by the presence of additional I_3^- when the perovskite phases are formed. Dominant deep-level defects (A1 and A2) and semishallow defects (A3) with energy levels of 0.78 to 0.82 eV and 0.46 eV below the conduction band, respectively, have not yet been experimentally identified but may be associated with defect states originating from interstitial Pb (Pb_i) and antisite defects (MA_I, Pb_I, I_{MA}, and I_{Pb}) (*12*, *13*). Indeed, Buin *et al.* (*12*) theoretically predicted that these deep-level trap concentrations would be affected by changes in the concentration of iodide anions and calculated the energy levels of I_{Pb}, Pb_I, and Pb defects.

The target layer exhibited an increase in PL intensity of ~225% relative to the control layer for excitation at 620 nm (fig. S6) (*25*). The improvement in the PL intensity can be correlated to the difference (ΔV) in the V_{oc} measured from the *J-V* characteristics, as described in the supplementary materials, suggesting that I_3^- decreases the numbers of deep-level traps within bulk perovskite layers. The carrier dynamics derived from the transient PL behavior provides information of charge recombination via nonradiative recombination related to the defect concentration. The PL decay (Fig. 2B) measured by time-correlated single-photon counting was fitted to a biexponential equation: $Y = A_1\exp(-t/\tau_1) + A_2\exp(-t/\tau_2)$ (*30*). We attributed quenching of the short PL lifetime to defect-induced nonradiative recombination and of the long PL lifetime to radiative recombination (*31*, *32*). The target layer displays a PL lifetime of ~138 ns and a long carrier lifetime of ~1105 ns, whereas the control layer exhibits PL lifetimes of ~72 ns and ~228 ns, respectively. The longer lifetime of the PL transition in the target layer may be attributed to the decrease in the concentration of defects and the increase in crystallinity. In addition, the PL quantum efficiency (PLQE) as a function of excitation power for the radiative and nonradiative recombination is higher in the target layer at all light intensities [fig. S7 (*25*)] (*33*–*35*).

On the basis of these results, we repeated the fabrication procedure to further enhance the PSC performance, using the tuned dripping solution in a two-step process. The *J-V* curves presented in Fig. 3A were determined for one of the most efficient cells, measured with a 50-ms scanning delay in both reverse- and forward-scan modes under standard air-mass 1.5 global (AM 1.5 G) illumination. The *J-V* curves show no appreciable hysteresis between the two modes. The J_{sc}, V_{oc}, and FF values obtained from the *J-V* curve in the reverse-scan mode were 25.0 mA·cm^{-2}, 1.11 V, and 0.817, respectively, yielding a PCE of 22.6% under standard AM 1.5 G conditions. The corresponding values obtained from the *J-V* curve in the forward-scan mode were 25.0 mA·cm^{-2}, 1.10 V, and 0.805, respectively, yielding a similar overall efficiency of 22.2%. For certification purposes, these representative devices were sent to the independent laboratory, which revealed an overall efficiency of 22.1% for the best-performing cell (fig. S8) (*25*), the highest efficiency ever reported for a PSC. The efficiency of this cell was maintained at >93% of the initial value after ~13 months of storage at ambient conditions (fig. S9) (*25*).

We prepared 80 cells independently under the same experimental conditions. The histogram of the average PCEs (Fig. 3B) shows that ~90% of the cells had PCEs exceeding 20.0% under 1-sun illumination with an average efficiency of 21.25 ± 1.08%. We also fabricated cells with active areas of ~1 cm^2 to check the uniformity of the perovskite layers produced using the above-described methodology. The *J-V* curve determined as an average of the reverse and the forward scans with corresponding J_{sc}, V_{oc}, and FF values of 24.2 mA cm^{-2}, 1.14 mV, and 72.7%, respectively, achieving an overall PCE of 20.0% under standard AM 1.5 G conditions (Fig. 3C); the certified performance was 19.7% under AM 1.5 G full-sun conditions (fig. S10) (*25*). The slight decrease in the performance of the large cell relative to that of smaller cells can be attributed to the large sheet resistance of the FTO substrate. This study demonstrates that careful control of the growth conditions of perovskite layers with management of deficient halide anions is essential for realizing high-efficiency thin-film PSCs based on lead-halide-perovskite absorbers.

REFERENCES AND NOTES

1. S. S. Shin *et al.*, *Science* **356**, 167–171 (2017).
2. Q. Jiang *et al.*, *Nat. Energy* **2**, 16177 (2017).
3. M. Saliba *et al.*, *Science* **354**, 206–209 (2016).
4. M. Saliba *et al.*, *Energy Environ. Sci.* **9**, 1989–1997 (2016).
5. W. S. Yang *et al.*, *Science* **348**, 1234–1237 (2015).
6. J. H. Heo *et al.*, *Nat. Photonics* **7**, 486–491 (2013).
7. N. J. Jeon *et al.*, *Nat. Mater.* **13**, 897–903 (2014).

8. N. J. Jeon *et al.*, *Nature* **517**, 476–480 (2015).
9. J. H. Noh, S. I. Seok, *MRS Bull.* **40**, 648–653 (2015).
10. G. E. Eperon *et al.*, *Energy Environ. Sci.* **7**, 982–988 (2014).
11. A. Buin, R. Comin, J. Xu, A. H. Ip, E. H. Sargent, *Chem. Mater.* **27**, 4405–4412 (2015).
12. A. Buin *et al.*, *Nano Lett.* **14**, 6281–6286 (2014).
13. W.-J. Yin, T. Shi, Y. Yan, *Appl. Phys. Lett.* **104**, 063903 (2014).
14. Q. Chen *et al.*, *Nano Lett.* **14**, 4158–4163 (2014).
15. R. J. Stewart, C. Grieco, A. V. Larsen, J. J. Maier, J. B. Asbury, *J. Phys. Chem. Lett.* **7**, 1148–1153 (2016).
16. N. K. Noel *et al.*, *ACS Nano* **8**, 9815–9821 (2014).
17. J. Xu *et al.*, *Nat. Commun.* **6**, 7081 (2015).
18. N. De Marco *et al.*, *Nano Lett.* **16**, 1009–1016 (2016).
19. E. Edri *et al.*, *Nat. Commun.* **5**, 3461 (2014).
20. J. S. Yun *et al.*, *J. Phys. Chem. Lett.* **6**, 875–880 (2015).
21. D. Bi *et al.*, *Sci. Adv.* **2**, e1501170 (2016).
22. R. J. Stewart, C. Grieco, A. V. Larsen, G. S. Doucette, J. B. Asbury, *J. Phys. Chem. C* **120**, 12392–12402 (2016).
23. J. Cao *et al.*, *J. Am. Chem. Soc.* **138**, 9919–9926 (2016).
24. A. Manglik, S. Sharma, V. Kudesia, *React. Kinet. Catal. Lett.* **15**, 467–473 (1981).
25. Materials and methods are available as supplementary materials.
26. J. M. Gardner, M. Abrahamsson, B. H. Farnum, G. J. Meyer, *J. Am. Chem. Soc.* **131**, 16206–16214 (2009).
27. J. M. Ball, A. Petrozza, *Nat. Energy* **1**, 16149 (2016).
28. T. J. Jacobsson *et al.*, *J. Am. Chem. Soc.* **138**, 10331–10343 (2016).
29. S. Heo *et al.*, *Sci. Rep.* **6**, 30554 (2016).
30. Q. Han *et al.*, *Adv. Mater.* **28**, 2253–2258 (2016).
31. S. D. Stranks *et al.*, *Phys. Rev. Appl.* **2**, 034007 (2014).
32. L. M. Herz, *Annu. Rev. Phys. Chem.* **67**, 65–89 (2016).
33. W. Zhang *et al.*, *Nat. Commun.* **6**, 10030 (2015).
34. X. Wen *et al.*, *J. Phys. Chem. C* **4**, 793–800 (2016).
35. J. T.-W. Wang *et al.*, *Energy Environ. Sci.* **9**, 2892–2901 (2016).

ACKNOWLEDGMENTS

This work was supported by the Global Frontier R&D (Research and Development) Program of the Center for Multiscale Energy System (NRF-2011-0031565 and NRF-2016M3A6A7945503) and the Climate Change Program (NRF-2015M1A2A2056542) through the National Research Foundation of Korea (NRF) funded by the Ministry of Science, ICT (Information and Communication Technology) and Future Planning. This work was also supported by a brand project (1.170003.01) of the Ulsan National Institute of Science and Technology (UNIST) and internal project (no. KK1702-A01) of the Korea Research Institute of Chemical Technology (KRICT). The GIWAXS experiment at the PLS-II 6D UNIST–Pohang Accelerator Laboratory beamline was supported in part by the Ministry of Education, Science, and Technology; Pohang University of Science and Technology; and UNIST–Central Research Facilities Center. We thank Tae Joo Shin for the indexing of 2D GIWAXS patterns. N.J.J. acknowledges financial support from the Basic Science Research Program (NRF-2015R1A6A3A04058164). All results are reported in the main text and supplementary materials. W.S.Y., J.H.N., J.S., and S.I.S. are inventors on patent application (KR 10-2016-0097290) submitted by both UNIST and KRICT that covers the preparation of perovskite films.

SUPPLEMENTARY MATERIALS

www.sciencemag.org/content/356/6345/1376/suppl/DC1
Materials and Methods
Figs. S1 to S10
References (*36*–*38*)

14 March 2017; accepted 31 May 2017
10.1126/science.aan2301

Science

Iodide management in formamidinium-lead-halide–based perovskite layers for efficient solar cells

Woon Seok Yang, Byung-Wook Park, Eui Hyuk Jung, Nam Joong Jeon, Young Chan Kim, Dong Uk Lee, Seong Sik Shin, Jangwon Seo, Eun Kyu Kim, Jun Hong Noh and Sang Il Seok

Science **356** (6345), 1376-1379.
DOI: 10.1126/science.aan2301

Healing defects with triiodide ions

Deep-level defects in organic-inorganic perovskites decrease the performance of solar cells through unproductive recombination of charge carriers. Yang *et al.* show that introducing additional triiodide ions during the formation of layers of formamidinium lead iodide, which also contain small amounts of methylammonium lead bromide, suppresses the formation of deep-level defects. This process boosts the certified efficiency of 1-cm^2 solar cells to almost 20%.

Science, this issue p. 1376